Available online at www.sciencedirect.com
SCIENCE DIRECT®
Journal of Computational Physics 193 (2003) 1–20
JOURNAL OF COMPUTATIONAL PHYSICS
www.elsevier.com/locate/jcp

Extending Gal-Chen and Somerville terrain-following coordinate transformation on time-dependent curvilinear boundaries

Nils P. Wedi [a,*], Piotr K. Smolarkiewicz [b]

[a] European Centre for Medium Range Weather Forecasts (ECMWF), Shinfield Park, Reading RG2 9AX, UK
[b] National Center for Atmospheric Research, Boulder, CO 80307, USA

Received 28 February 2003; received in revised form 17 July 2003; accepted 17 July 2003

Abstract

The classical terrain-following coordinate transformation of Gal-Chen and Somerville has been extended to a broad class of time-dependent vertical domains. We provide explicit formulae for the associated transformation coefficients which are readily applicable to numerical implementations. The proposed extension facilitates modeling of undulating boundaries in various areas of computational fluid dynamics. The implementation is discussed in the context of a nonhydrostatic anelastic model for simulations of atmospheric and oceanic flows. The theoretical development is illustrated with numerical simulations of idealized flows. We also discuss an example of a practical application which incorporates a long-wave-approximation for a finite-amplitude free-surface upper boundary, directly relevant to ocean models.

Keywords: Gal-Chen and Somerville; Time-dependent coordinate transformation; Ocean; Atmosphere; Boundary conditions; Free surface

1. Introduction

In meteorology, continuous coordinate transformations using a general curvilinear framework are favored, simplifying theories and models by reflecting the natural material structure of atmospheres and oceans [12]. The latter exploits the notion of a "metric structure determined by data" – Riemann's seminal idea on the foundations of geometry [43], an inspiration behind the mathematical apparatus of general relativity [13]. For example, the density stratification and near hydrostatic balance of the Earth atmosphere favor pressure as a vertical coordinate of weather prediction models, assuring an approximate equipartition of mass and energy in computational cells [24,29,37]. Similarly, the stable entropy [density] stratification in

* Corresponding author. Tel.: +44-118-949-9657; fax: +44-118-986-9450.
E-mail addresses: wedi@ecmwf.int (N.P. Wedi), smolar@ncar.ucar.edu (P.K. Smolarkiewicz).

0021-9991/$ - see front matter
doi:10.1016/j.jcp.2003.07.034

deep atmospheres [oceans] makes an isentropic [isopycnic] framework practical [2,3,19,20]. Attempts to exploit the advantages of different curvilinear frameworks for various regions of a simulated atmosphere [ocean] have led to pressure- or entropy-based coordinate hybridization [27,46,57,59]. The majority of currently-operational numerical weather prediction models are formulated in hybrid coordinates.

An important property of curvilinear coordinates is their ability to accomodate domains with irregular boundaries. In meteorology, these are typically associated with complex natural orography [bathymetry]. The accurate representation of the underlying metric structure is particularly important for modeling stably stratified rotating media, where the boundary forcing excites internal inertia-gravity waves affecting the far-field flow. For example, the (non-Boussinesq) amplification of vertically propagating gravity waves can lead to clear-air turbulence (via wave steepening and subsequent breaking) in the middle atmosphere [39]. Weather prediction models have traditionally used pressure normalized by surface pressure in the definition of the "vertical" coordinate to represent accurately the influence of the terrain variability on large-scale planetary flows [37]. Gal-Chen and Somerville [5] were the first to incorporate terrain-following curvilinear coordinates in the nonhydrostatic anelastic Navier–Stokes equations appropriate for small-scale atmospheric and oceanic flows. They transformed a linear vertical coordinate (as opposed to pressure) and provided closed-form explicit formulae for the relevant metric terms and coefficients. By construction, their transformation separates all metric coefficients into products of 2D horizontal and 1D vertical fields, facilitating a computationally efficient implementation.

The Gal-Chen and Somerville development employed the classical coordinate-invariant tensor representation (a "weak-conservation formulation") where the consistently transformed, dependent variables are solved in the framework of the transformed coordinates. While the invariance of the formulation is beneficial in theory, it has considerable disadvantages in the numerical implementation. Due to Christoffel terms arising in the transformed momentum equation, the conservation of physical (measurable) kinematic variables may be difficult to achieve. Furthermore, since Christoffel terms represent inertial accelerations due to the curvilinearity of the coordinates, they only affect flow direction but not the flow magnitude. To minimize truncation-error departures from this "inertness" in numerical algorithms, it is important to express the Christoffel terms centered-in-time. While straightforward in three-time-level centered-in-time-and-space (leapfrog) schemes, this leads in two-time level algorithms (forming the base of modern nonoscillatory methods) to an implicit nonlinear problem. Both issues are circumvented in the "strong-conservation formulation" advocated by Clark [9] – a standard in computational aerodynamics [1] – where the governing equations are solved in the framework of Gal-Chen and Somerville transformed coordinates, but for the untransformed physical velocity. However, the strong-conservation formulation adds some conceptual complexity in incompressible type models, due to the presence of several forms of velocity and an elaborate procedure for formulating the elliptic pressure equation [40]. The early contributions of Gal-Chen and Somerville [5] and Clark [9] were fundamental to the development of many small- and mesoscale models in meteorology (over 500 citations since 1975; [23]). More recently, the stationary terrain-following transformation of Gal-Chen and Somerville was extended in [39] to allow for time-dependent lower boundaries.

The importance of an accurate representation of the upper boundary condition in meteorological models is well appreciated since it affects short- and medium-range weather prediction [30,38], climate studies [58], and predictability of chaotic systems in general [8]. However, a unified numerical framework to investigate the influence of various upper boundary assumptions does not exist, because each model formulation favors a particular type of the upper boundary. For example, it is easy to impose a free-surface boundary condition in an isopycnic/isentropic model, but it is rather difficult to impose a rigid lid, easily applied in linear coordinates. Furthermore, there is an outstanding issue with modeling open boundaries that eludes a satisfactory solution in many areas of computational physics; cf. [15] and references therein. [1] In particular,

[1] For implementations of radiative boundary conditions in meteorology see [4,18,25].

Grosch and Orszag [17] investigated the utility of coordinate transformations to solve numerically problems in infinite regions. They concluded that stationary mappings onto finite domains are "useless for many important physical problems."

In this paper, we generalize the time-dependent extension [39] of the Gal-Chen and Somerville transformation for curvilinear time-dependent boundaries at the top as well as the bottom of the model domain. We provide explicit formulae for the relevant metric coefficients and discuss the implementation in the context of a strong-conservation formulation of the nonhydrostatic anelastic equations of Lipps and Hemler [31]. Our aim is to create a unified numerical framework for investigating the influence of upper boundary conditions on atmospheric and oceanic flows. In technical terms, this paper enhances the adaptivity of numerical models to boundary forcings determined by data.

To illustrate both aspects, we compare simulations of an orographic flow in a homogeneous incompressible fluid (bounded by a rigid-lid or by a finite-amplitude free-surface) with the simulation of an incompressible two-layer fluid with a density ratio 1/1000 at the interface. In the simulation with the free-surface, our time-dependent coordinate transformation is driven by the solution of the shallow-water equations, a low-order long-wave approximation to free-surface flows. The physics of this example is relevant to ocean models. In numerical simulations of ocean circulations "mode splitting" is often applied to accomodate surface gravity waves with propagation speeds much larger than velocities of internal flows [19,32]. Our development provides an alternative for incorporating a finite-amplitude free surface upper boundary in ocean models.

The paper is organized as follows. In the next section, we summarize the anelastic model equations in a general curvilinear framework, introduce explicit metric coefficients resulting from our specific coordinate transformation and outline the numerical solution procedure. In Section 3, we provide examples of applications relevant to a few distinct areas of computational fluid dynamics, validating both the conceptual and numerical aspects of our approach. Remarks in Section 4 conclude the paper.

2. The anelastic model and coordinate transformation

2.1. Model summary

We discuss an inviscid, adiabatic, density-stratified fluid whose undisturbed, balanced ambient (or environmental) state is described by the potential temperature $\theta_e = \theta_e(\mathbf{x})$ and the velocity $\mathbf{v}_e = \mathbf{v}_e(\mathbf{x})$. A comprehensive discussion of our anelastic model can be found in [40] and references therein. To facilitate the distinction between physical aspects of the anelastic system versus mathematical aspects of the transformation, we start with a compact, symbolic vector-form of the anelastic equations [31]

$$\begin{aligned} &\nabla\cdot(\rho_b\mathbf{v}) = 0,\\ &\frac{D\mathbf{v}}{Dt} = -\nabla\pi' - \mathbf{g}\frac{\theta'}{\theta_b} + \mathbf{F},\\ &\frac{D\theta'}{Dt} = -\mathbf{v}\cdot\nabla\theta_e. \end{aligned} \tag{1}$$

Here, the operators D/Dt, ∇, and $\nabla\cdot$ symbolize the material derivative, gradient, and divergence; $\mathbf{v}$ denotes the velocity vector; $\mathbf{F}$ symbolizes inertial forces (e.g., Coriolis and metric forces of the geo-spherical physical system, cf. [52]); [2] θ, ρ, and π denote potential temperature, density, and a density-normalized pressure; and

[2] In general, $\mathbf{F}$ will also include viscous and external forcings.

g symbolizes the gravity vector. Primes denote deviations from the environmental state. The subscript $_{\mathrm{b}}$ refers to the basic state, i.e., a horizontally homogeneous hydrostatic reference state of the Boussinesq expansion around a constant stability profile (see Section 2a in [10], for a discussion). For the reader's convenience, all symbols used throughout the paper are tabulated in Table 2.

We embed our time-dependent coordinate transformation into the theoretical framework of [40], where the authors considered a general three dimensional, time-variable homeomorphic mapping from a physical system [3] $(t,\mathbf{x})$ to an arbitrary $(\bar{t},\overline{\mathbf{x}})$

$$(\bar{t},\bar{x},\bar{y},\bar{z}) \equiv (t, E(x,y,t), D(x,y,t), C(x,y,z,t)). \tag{2}$$

Since $(\bar{x},\bar{y})$ do not depend upon the vertical coordinate z – preserving the primary hydrostatic structure of atmospheres and oceans, and simplifying the metric terms – our development of a particular $C(x,y,z,t)$ readily applies.

Given (2), the symbolic vector-form Eq. (1) can be expressed as

$$\begin{aligned}
&\frac{\partial(\rho^*\overline{v^s}^k)}{\partial\bar{x}^k} = 0,\\
&\frac{\mathrm{d}v^j}{\mathrm{d}\bar{t}} = -\widetilde{G}^k_j\frac{\partial\pi'}{\partial\bar{x}^k} + g\frac{\theta'}{\theta_{\mathrm{b}}}\delta^j_3 + F^j,\\
&\frac{\mathrm{d}\theta'}{\mathrm{d}\bar{t}} = -\overline{v^s}^k\frac{\partial\theta_{\mathrm{e}}}{\partial\bar{x}^k}.
\end{aligned} \tag{3}$$

Here, $\rho^* := \rho_{\mathrm{b}}\overline{G}$, with $\overline{G}$ denoting the Jacobian of the transformation, and $j,k = 1,2,3$ correspond to the $\bar{x},\bar{y},\bar{z}$ components, respectively. Summation is implied by repeated indices, unless stated otherwise. On the rhs of the momentum equation, $\widetilde{G}^k_j := \sqrt{g^{jj}}(\partial\bar{x}^k/\partial x^j)$ are renormalized elements of the Jacobian (summation not implied over j); the coefficients g^{jj} are the diagonal elements of the conjugate metric tensor of the (not necessarily Cartesian) physical system $(t,\mathbf{x})$, [4] and δ^j_3 is the Kronecker delta. The transformation coefficients $\widetilde{G}^k_j \neq \widetilde{G}^j_k$ are not to be confused with the elements of the metric tensor of the transformation $\overline{g}^{jk} = \overline{g}^{kj} = g^{pq}(\partial\bar{x}^k/\partial x^p)(\partial\bar{x}^j/\partial x^q)$ with $\overline{G} = \mid \overline{g}^{jk} \mid^{-1/2}$. Furthermore, three different representations of velocity appear in (3). In the material derivative $\mathrm{d}/\mathrm{d}\bar{t} = \partial/\partial\bar{t} + \overline{v^*}^k(\partial/\partial\bar{x}^k)$, the *contravariant velocity* $\overline{v^*}$ is used

$$\overline{v^*}^k := \mathrm{d}\bar{x}^k/\mathrm{d}\bar{t} := \dot{\bar{x}}^k; \tag{4}$$

whereas on the lhs of the momentum equation, the *physical velocity* v^j, specified in the physical system $(t,\mathbf{x})$, is advected by $\overline{v^*}^k$. The *solenoidal velocity* appearing in the mass continuity and potential temperature equations is given as

$$\overline{v^s}^k := \overline{v^*}^k - \frac{\partial\bar{x}^k}{\partial t}, \tag{5}$$

with the name originating from the form the continuity equation takes with it. The relations, allowing to express each velocity (solenoidal, contravariant, or physical) in terms of the others, have been discussed in [40]. The two relations important for the numerical solution procedure are (5) and

$$\overline{v^s}^j = \widetilde{G}^j_n v^n. \tag{6}$$

[3] Only curvilinear coordinate descriptions of a flat (locally Lorentz) space with a zero Riemann curvature tensor are considered.

[4] The components of the conjugate metric tensor follow from the definition of the fundamental metric $\mathrm{d}s^2 = g_{pq}\mathrm{d}x^p\mathrm{d}x^q$ and the linear system $g_{pk}g^{kq} \equiv \delta^q_p$, cf. [40].

The simultaneous use of the contravariant and the physical velocity eliminates Christoffel terms of the transformation (proportional to products of contravariant velocity components) from the momentum equation; the use of the solenoidal velocity is advantageous while formulating the elliptic pressure equation [41].

2.2. Generalized Gal-Chen and Somerville vertical coordinate

Starting from the physical system $(t,\mathbf{x})$, we collapse the general dependence of $\overline{z}$ on (x,y,z,t) in (2) into a similarity transformation

$$\begin{aligned}\overline{z} &= C(\xi),\\ \xi &= \xi(x,y,z,t) := H_0\frac{z-z_s(x,y,t)}{H(x,y,t)-z_s(x,y,t)},\end{aligned} \tag{7}$$

with the inverse relationship

$$\begin{aligned}z &= \frac{\xi}{H_0}(H-z_s)+z_s,\\ \xi &= C^{-1}(\overline{z}).\end{aligned} \tag{8}$$

The function C conveniently admits a class of vertically stretched coordinates. In particular, it allows to simulate the vertical coordinate spacing of pressure or sigma levels [56], common in atmospheric or oceanic applications. The transformation in (7) retains the computational advantage of separability into one- and two-dimensional fields. In particular, the Jacobian of the transformation is given as

$$\overline{G} = \left(\frac{\mathrm{d}C}{\mathrm{d}\xi}\frac{\partial\xi}{\partial z}\right)^{-1}\left(\frac{\partial E}{\partial x}\frac{\partial D}{\partial y}-\frac{\partial E}{\partial y}\frac{\partial D}{\partial x}\right)^{-1} \equiv \left(\frac{\mathrm{d}C}{\mathrm{d}\xi}\right)^{-1}\overline{G}_0\overline{G}_{xy}, \tag{9}$$

with

$$\overline{G}_0 \equiv \left(\frac{\partial\xi}{\partial z}\right)^{-1} = \frac{H(x,y,t)-z_s(x,y,t)}{H_0}, \tag{10}$$

reminiscent of the original Gal-Chen and Somerville Jacobian.

The transformation coefficients $\widetilde{G}^k_j$ – defined following (3) – affected by the vertical transformation (7) are

$$\begin{aligned}\widetilde{G}^3_1 &= \sqrt{g^{11}}\frac{\mathrm{d}C}{\mathrm{d}\xi}\frac{\partial\xi}{\partial x},\\ \widetilde{G}^3_2 &= \sqrt{g^{22}}\frac{\mathrm{d}C}{\mathrm{d}\xi}\frac{\partial\xi}{\partial y},\\ \widetilde{G}^3_3 &= \sqrt{g^{33}}\frac{\mathrm{d}C}{\mathrm{d}\xi}\frac{\partial\xi}{\partial z},\end{aligned} \tag{11}$$

where

$$\begin{aligned}\frac{\partial\xi}{\partial x} &= \frac{1}{\overline{G}_0}\left[\frac{\partial z_s}{\partial x}\left(\frac{z-H}{H-z_s}\right)-\frac{\partial H}{\partial x}\left(\frac{z-z_s}{H-z_s}\right)\right],\\ \frac{\partial\xi}{\partial y} &= \frac{1}{\overline{G}_0}\left[\frac{\partial z_s}{\partial y}\left(\frac{z-H}{H-z_s}\right)-\frac{\partial H}{\partial y}\left(\frac{z-z_s}{H-z_s}\right)\right],\\ \frac{\partial\xi}{\partial z} &= \frac{1}{\overline{G}_0}.\end{aligned} \tag{12}$$

To solve the governing Eq. (3) in the transformed space, the coefficients $\widetilde{G}^k_j$ must be expressed as functions of $(\overline{t},\overline{\mathbf{x}})$. In numerical models using the Gal-Chen and Somerville transformation, the coefficients (12) are typically evaluated using a direct differentiation of $z_s(x,y)$. From our experience, however, we find an alternative approach, tailored to the numerical differentiation of $\overline{G}_0$, computationally beneficial (e.g., for minimizing spurious vorticity generation at free-slip boundaries). We start with defining

$$\begin{aligned}
h_{13} &:= \frac{1}{\overline{G}_0}\frac{\partial H}{\partial x} = \left[\frac{1}{\overline{G}_0}\frac{\partial H}{\partial \overline{x}}\right]\frac{\partial E}{\partial x} + \left[\frac{1}{\overline{G}_0}\frac{\partial H}{\partial \overline{y}}\right]\frac{\partial D}{\partial x},\\
h_{23} &:= \frac{1}{\overline{G}_0}\frac{\partial H}{\partial y} = \left[\frac{1}{\overline{G}_0}\frac{\partial H}{\partial \overline{x}}\right]\frac{\partial E}{\partial y} + \left[\frac{1}{\overline{G}_0}\frac{\partial H}{\partial \overline{y}}\right]\frac{\partial D}{\partial y},\\
s_{13} &:= \frac{1}{\overline{G}_0}\frac{\partial \overline{G}_0}{\partial x} = \left[\frac{1}{\overline{G}_0}\frac{\partial \overline{G}_0}{\partial \overline{x}}\right]\frac{\partial E}{\partial x} + \left[\frac{1}{\overline{G}_0}\frac{\partial \overline{G}_0}{\partial \overline{y}}\right]\frac{\partial D}{\partial x},\\
s_{23} &:= \frac{1}{\overline{G}_0}\frac{\partial \overline{G}_0}{\partial y} = \left[\frac{1}{\overline{G}_0}\frac{\partial \overline{G}_0}{\partial \overline{x}}\right]\frac{\partial E}{\partial y} + \left[\frac{1}{\overline{G}_0}\frac{\partial \overline{G}_0}{\partial \overline{y}}\right]\frac{\partial D}{\partial y}.
\end{aligned} \tag{13}$$

The formulae in (13) are written as implemented in the numerical model, with the [ ] terms referring to the numerical differentiation. [5] Second, we note that the definition of $\overline{G}_0$ in (10) implies

$$\begin{aligned}
\frac{1}{\overline{G}_0}\frac{\partial \overline{G}_0}{\partial x} &= \frac{1}{H-z_s}\left(\frac{\partial H}{\partial x} - \frac{\partial z_s}{\partial x}\right),\\
\frac{1}{\overline{G}_0}\frac{\partial \overline{G}_0}{\partial y} &= \frac{1}{H-z_s}\left(\frac{\partial H}{\partial y} - \frac{\partial z_s}{\partial y}\right),\\
\frac{1}{\overline{G}_0}\frac{\partial \overline{G}_0}{\partial t} &= \frac{1}{H-z_s}\left(\frac{\partial H}{\partial t} - \frac{\partial z_s}{\partial t}\right).
\end{aligned} \tag{14}$$

Manipulating (12), (14), and the definitions (13), the coefficients (11) are expressed solely in $(\overline{t},\overline{\mathbf{x}})$

$$\begin{aligned}
\widetilde{G}^3_1 &= \sqrt{g^{11}}\frac{\mathrm{d}C}{\mathrm{d}\xi}\left[s_{13}\left(H_0 - C^{-1}(\overline{z})\right) - h_{13}\right],\\
\widetilde{G}^3_2 &= \sqrt{g^{22}}\frac{\mathrm{d}C}{\mathrm{d}\xi}\left[s_{23}\left(H_0 - C^{-1}(\overline{z})\right) - h_{23}\right],\\
\widetilde{G}^3_3 &= \sqrt{g^{33}}\frac{\mathrm{d}C}{\mathrm{d}\xi}\frac{1}{\overline{G}_0}.
\end{aligned} \tag{15}$$

The *kinematic boundary condition* at an impermeable (e.g. material) surface (at the top, $\mathrm{d}H/\mathrm{d}t = w$, or at the bottom boundary, $\mathrm{d}z_s/\mathrm{d}t = w$; cf. [28]) follows from $\dot{\overline{x}}^3 \equiv 0$ in (4), hence specifying the boundary conditions for the solenoidal velocity defined in (5). Given all transformation coefficients and $\partial\overline{x}^k/\partial t$ expressed in transformed coordinates, the solenoidal velocity components are readily determined from (6), while the contravariant velocity components $\overline{v^*}^j$ defined in (4) are determined from (5). Manipulating the third relationship in (14), the inverse transformation (8), and the definition of $\overline{G}_0$ in (10), the derivative

$$\frac{\partial \xi}{\partial t} = \frac{1}{\overline{G}_0}\left[\frac{\partial z_s}{\partial t}\left(\frac{z-H}{H-z_s}\right) - \frac{\partial H}{\partial t}\left(\frac{z-z_s}{H-z_s}\right)\right], \tag{16}$$

is expressed in $(\overline{t},\overline{\mathbf{x}})$

[5] The elements of the Jacobi matrix $\partial(E,D)/\partial(x,y)$ are evaluated in $(\overline{t},\overline{\mathbf{x}})$ by computing the inverse of the Jacobi matrix $\partial(x,y)/\partial(\overline{x},\overline{y})$.

$$\frac{\partial \xi}{\partial t} = \frac{1}{\overline{G}_0}\frac{\partial \overline{G}_0}{\partial t}(H_0 - C^{-1}(\overline{z})) - \frac{1}{\overline{G}_0}\frac{\partial H}{\partial t}, \tag{17}$$

leading to the boundary conditions for the solenoidal velocity

$$\left\{ \overline{v}^3 = -\frac{\mathrm{d}C}{\mathrm{d}\xi}\left[\frac{1}{\overline{G}_0}\frac{\partial \overline{G}_0}{\partial t}(H_0 - C^{-1}(\overline{z})) - \frac{1}{\overline{G}_0}\frac{\partial H}{\partial t}\right] \right\}_{\overline{z}=0,H_0}. \tag{18}$$

For nontrivial horizontal transformations, the Jacobian (9) and all relations in (11)–(15) contain multiplicative factors that are only functions of $(\overline{x},\overline{y},\overline{t})$, uniquely determined from $\overline{x} = E(x,y,t)$ and $\overline{y} = D(x,y,t)$. In [40] the authors focused on horizontal transformations for mesh adaptivity. In the following examples we assume the identity transformation in the horizontal, $\overline{x} \equiv x$ and $\overline{y} \equiv y$, since it does not compromise the generality of the approach (2) while stressing the utility of the generalized Gal-Chen and Somerville vertical coordinate in (7). Furthermore, the stretching function $C(\xi)$ is taken as the identity in the examples. Consequently, $\widetilde{G}^2_1 = \widetilde{G}^1_2 = \widetilde{G}^1_3 = \widetilde{G}^2_3 = 0$ and $\widetilde{G}^1_1 = \widetilde{G}^2_2 = 1$, while h_{ij} and s_{ij} are simplified accordingly.

2.3. The numerical approximation

The nonhydrostatic anelastic Eq. (3) are solved numerically using a second-order-accurate nonoscillatory forward-in-time (NFT) approach, broadly documented in the literature. Below we comment briefly on the essential aspects of the numerical solution procedure while referring the reader to earlier works for further details.

The prognostic equations in (3) can be written in a compact conservation-law form

$$\frac{\partial \rho^* \psi}{\partial \overline{t}} + \overline{\nabla}\cdot(\rho^* \overline{\mathbf{v}}^* \psi) = \rho^* R, \tag{19}$$

where $\overline{\nabla} := (\partial/\partial\overline{x}, \partial/\partial\overline{y}, \partial/\partial\overline{z})$, and ψ symbolizes a velocity component or potential temperature. In (19), R summarizes the rhs of the equations in (3). Alternatively, the same prognostic equations can be formulated in Lagrangian form

$$\frac{\mathrm{d}\psi}{\mathrm{d}\overline{t}} = R. \tag{20}$$

On a discrete mesh, the NFT approximation of either formulation – flux-form Eulerian [50] for (19), or semi-Lagrangian [49] for (20) – can be written compactly as

$$\psi^{n+1}_{\mathbf{i}} = \mathrm{LE}_{\mathbf{i}}(\widetilde{\psi}) + 0.5\Delta t R^{n+1}_{\mathbf{i}}. \tag{21}$$

Here, we denote $\psi^{n+1}_{\mathbf{i}}$ as the solution at the grid point $(\overline{t}^{n+1}, \overline{\mathbf{x}}_{\mathbf{i}})$; $\widetilde{\psi} := \psi^n + 0.5\Delta t R^n$; and LE denotes a NFT transport operator. In the Eulerian scheme, LE integrates the homogeneous transport Eq. (19), i.e., LE advects $\widetilde{\psi}$ using a fully second-order-accurate multidimensional MPDATA advection scheme [53,55]. In the semi-Lagrangian algorithm, LE remaps transported fields, which arrive at the grid points $(\overline{t}, \overline{\mathbf{x}}_{\mathbf{i}})$, to the departure points of the flow trajectories $\left(\overline{t}^n, \overline{\mathbf{x}}_0(\overline{t}^{n+1}, \overline{\mathbf{x}}_{\mathbf{i}})\right)$ also using MPDATA type advection schemes [48,49].

The overall model algorithm (21) represents a system of equations implicit with respect to all dependent variables in (3), since all forcings $R^{n+1}_{\mathbf{i}}$ are assumed to be unknown at $n+1$. For the potential temperature equation, the rhs includes the complete convective derivative, ensuring an adequate treatment of the impermeability condition at the lower boundary and the conservation of θ', regardless of details of the transformation (2) (see [56], for discussions). The implicitness of the pressure gradient forces in the numerical approximation of the momentum equation conveniently enables the projection of preliminary

values $\mathrm{LE}(\widetilde{\psi})$ in (21) to solutions of the continuity equation in (3). First, the system of simultaneous equations resulting from (21) is algebraically inverted to construct expressions for the discrete solenoidal velocity components using (6). Then, the resulting solenoidal velocity is substituted in the discrete form of the mass continuity equation in (3), forming an elliptic equation for pressure (see Appendix A in [40] for the complete development). The elliptic pressure equation is solved (stressing the need for appropriate boundary conditions) using the generalized conjugate-residual approach – a preconditioned nonsymmetric Krylov-subspace solver [47,51,54]. Given the updated pressure, and hence the updated solenoidal velocity, the updated physical and contravariant velocity components are constructed from the solenoidal velocities inverting the relations in (6) and (5), respectively. Nonlinear terms in R^{n+1} (e.g., metric terms arising in a geo-spherical physical system) may require outer iteration of the system of equations generated by (21) – see the Appendix of [56] for a discussion.

3. Examples of applications

3.1. Overview

Here we supplement the theory of the preceding sections with three examples, validating both the conceptual and numerical aspects of our approach while illustrating the utility of the generalized vertical coordinate. In the first example, we illustrate in three spatial dimensions the use of time-dependent lower and upper boundaries with finite curvature, in the context of a homogeneous Boussinesq fluid enclosed by oscillating membranes. This demonstrates the capability to incorporate large amplitude boundary variations, testing the accuracy of the boundary conditions, which directly impact the convergence of the elliptic pressure solver. Furthermore, our approach complements biomedical numerical studies such as vascular flows, where an accurate description of a three-dimensional fluid flow bounded by undulating arterial walls is required, given accurate lateral boundary conditions already considered in [36]. The second example stresses the accuracy of our approach in the context of stably stratified atmospheric flows, supporting vertically propagating gravity waves, and shows the potential for alternative formulations of nonreflective upper boundaries. Finally, the third example illustrates the utility of the generalized Gal-Chen and Somerville coordinate transformation for numerical adaptivity to boundary forcings determined by data. In particular, we discuss an alternative for incorporating a finite-amplitude free-surface upper boundary in the context of a nonhydrostatic oceanic flow.

3.2. Boundary-forced oscillating flow

Initially stagnant, adiabatic 3D flow of a homogeneous Boussinesq fluid is forced by oscillating impermeable free-slip upper and lower boundaries, with their shape prescribed as

$$\begin{aligned} z_{\mathrm{s}}(r(x,y),t) &= \begin{cases} z_{\mathrm{s}0}\cos^2(\pi r/2L)\sin(2\pi t/T) & \text{if } r/L \leqslant 1, \\ 0 & \text{otherwise,} \end{cases} \\ H(x,y,t) &= H_0 - z_{\mathrm{s}}(x,y,t), \end{aligned} \tag{22}$$

with $r=\sqrt{x^2+y^2}$, oscillation period $T=48\Delta t$, amplitude $z_{\mathrm{s}0}=48\Delta z$, and the membranes' half-width $L=48\Delta x$, where $\Delta x=\Delta y=\Delta z$. The computational domain consists of $150\times150\times120$ grid intervals, in the horizontal and vertical, respectively. The advection scheme is semi-Lagrangian [49]. Note that after $t=T/4$, the upper and lower boundaries are separated merely by one fifth of the vertical extent of the model. In relation to geophysical scenarios, the present example is representative of steep (yet well resolved) orographies. The magnitude of the induced flow and its variation is approximately 5 and 0.5, respectively,

as measured by $\mathscr{C} \equiv \|\Delta t\overline{\mathbf{v}}^*/\Delta\overline{\mathbf{x}}\|$ and $\mathscr{L} \equiv \|\Delta t\partial\overline{\mathbf{v}}^*/\partial\overline{\mathbf{x}}\|$ – the (maximal) Courant and "Lipschitz" numbers (cf. [49] for a discussion).

Fig. 1 illustrates the results. The flow vectors with imposed contour lines of the normalized perturbation pressure π' are shown at two phases of the simulation ($t/T = 5/48$, and $t/T = 22/48$) which convey particularly well the reversing inward/outward flow patterns between the upward/downward oscillating membranes. Flow vectors are multiplied by $\Delta t/\Delta x$ to acquire the sense of local Courant numbers; whereas π' is multiplied by $2(\Delta t/\Delta x)^2$ relating to the squared lengths of the displayed vectors (via Bernoulli equation). Lacking diabatic forces, boundary friction, and buoyancy, the experimental setup implies a potential flow solution past oscillating membranes. The accuracy of the numerical solution can be assessed by examining the net pressure drag – i.e., the horizontal component of the integral pressure force on the bounding walls – that should vanish in consequence of the flow irrotationality (D'Alembert paradox, cf. section I.92 in [33]). [6] Indeed, the model predicted net drag is of the order of round-off errors. The rms error of residual vorticity ($\times\Delta t$), attributed primarily to the truncation errors of evaluating vorticity itself, is a few tenths of a percent of the flow variation measure $\mathscr{L}$. Finally, consider the Lagrangian form of the mass continuity equation $\rho^* = \rho_0^* J^{-1}$ – readily available in semi-Lagrangian models [56] – where ρ_0^* refers to ρ^* at the departure point $\overline{\mathbf{x}}_0$ of the trajectory arriving at a grid point $\overline{\mathbf{x}}$, and where J^{-1} denotes the inverse flow Jacobian, $J^{-1} \equiv |\,\partial\overline{\mathbf{x}}_0/\partial\overline{\mathbf{x}}\,|$. Subsequently, the density-normalized inverse flow Jacobian $\mathscr{J} := (\rho_0^*/\rho^* J^{-1}) \equiv 1$ can be employed to assess the accuracy of the computations. [7] The model predicted, domain-averaged values of $\mathscr{J}$ are between 0.99 and 1.01, with standard deviations 0.02–0.03. Summarizing, we have found this experiment a convenient tool to validate the correctness of implementation of the solenoidal velocity boundary conditions (implying Neumann boundary conditions for pressure), ensuring the integrability condition of the elliptic pressure equation.

3.3. Orographically-forced atmospheric gravity waves

To illustrate the accuracy and practicality of the generalized coordinate transformation for atmospheric applications, we consider a fully anelastic flow past a given terrain profile under stably stratified atmospheric conditions – a canonical problem in meteorological studies. We have simulated a suite of classical problems with flows past a bell-shaped mountain and compared them against identical but "upside-down" experiments with a bell-shaped valley at the upper boundary, gravity and stratification reversed. Such experiments validated the correctness of the generalized vertical coordinate, both theoretically and with respect to the numerical implementation.

In the following we show the special benchmark problem proposed recently by Schär et al. [45], stressing numerical implementations of the classical Gal-Chen and Somerville transformation in the limit of marginally resolved orographic features. The selected parameters of the problem favor bifurcation into a qualitatively incorrect solution [26]. To emphasize the robustness of our generalized transformation, we repeat the Schär et al. calculations while storing the instantaneous heights of a selected isentropic (material) surface, so as to create a time-dependent upper boundary for the subsequent simulation with approximately half the vertical extent. The terrain profile is given as

$$z_s(x) = z_{s0} \exp\left(\frac{-x^2}{a^2}\right) \cos^2\left(\frac{\pi x}{\lambda}\right), \tag{23}$$

[6] For a discussion of *form drag* in the geophysical context of stratified flows see sections 6.8 and 8.7 in [14]; for a derivation from the momentum budget cf. [11,60].

[7] In general, for a flow to be realizable (topological), $0 < \mathscr{J} < \infty$.

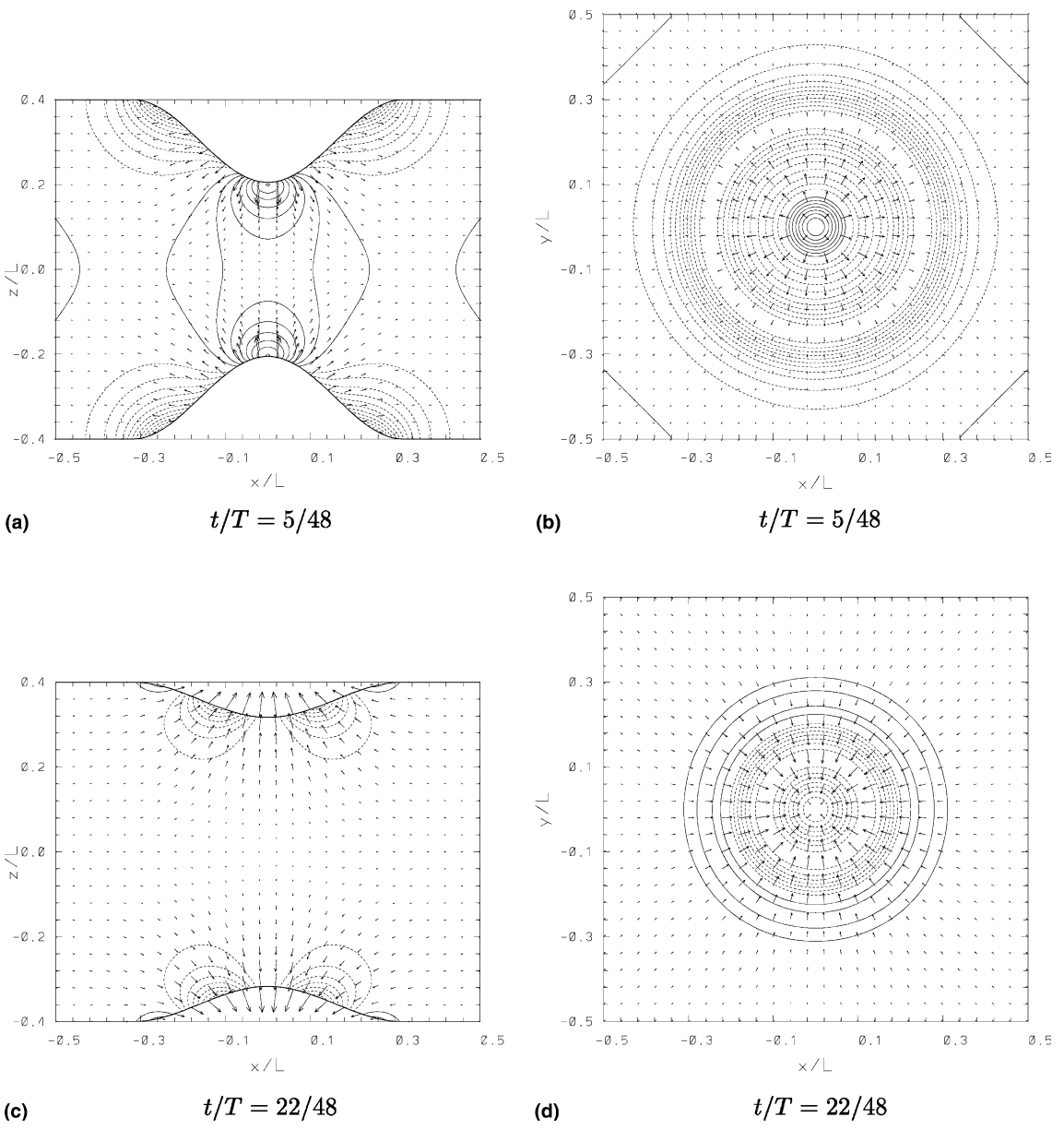

Fig. 1. Oscillating membranes bounding a homogeneous Boussinesq fluid. The figure shows the vectors of local Courant numbers and contour lines of the normalized pressure (see the text for the normalization details) in two distinct phases of the induced flow, outflow (plates a and b) and inflow (plates c and d). Plates (a) and (c) show vertical xz cross-sections at $y = 0$; whereas plates (b) and (d) display the solution at $z = z_s$, defined in (22). The contour intervals are 2 (zero contour lines are not shown), and the arrow length equal to the distance of two minor axis tickmarks is 4.

with $z_{s0} = 0.25$ km, $a = 5$ km and $\lambda = 4$ km. Ambient conditions consist of the uniform wind profile $u_e(z) = U = 10\ \mathrm{ms}^{-1}$ ($v_e = 0, w_e = 0$) and a Brunt–Väisällä frequency $N = 0.01\ \mathrm{s}^{-1}$. The domain is 70×21 km, with a horizontal and vertical grid spacing of 500 and 300 m, respectively. The integration time is 5 h

with a time step $\Delta t = 10$ s. The upper 11 km of the model domain are designated to an absorbing layer, to simulate an infinite atmosphere and to suppress spurious wave reflection from the upper rigid-lid. Lateral absorbers extend for 10 km away from the boundaries.

Fig. 2(a) shows the vertical velocity in the reference solution. This is the correct solution in agreement with the linear analytic result. For bifurcated, incorrect solutions see [26]. The result in Fig. 2(a) has been obtained using the Eulerian option of the model with the MPDATA advection scheme. However, the same results have been reproduced using the semi-Lagrangian option. The line in the figure at $z \approx 9.6$ km marks the height of an isentrope that has been extracted (by means of interpolation) and stored at each time step of the reference run. Here we exploit the material property (viz. impermeability) of isentropic surfaces in adiabatic flows, to create a time-dependent upper boundary condition for the finite domain simulation, without absorbing layer. This height data has been used in our coordinate transformation at each time step, to prescribe numerically $H(x,y,t)$ and $\partial H(x,y,t)/\partial t$. In (18), these determine uniquely the solenoidal velocity consistent with zero normal flow through the boundary.

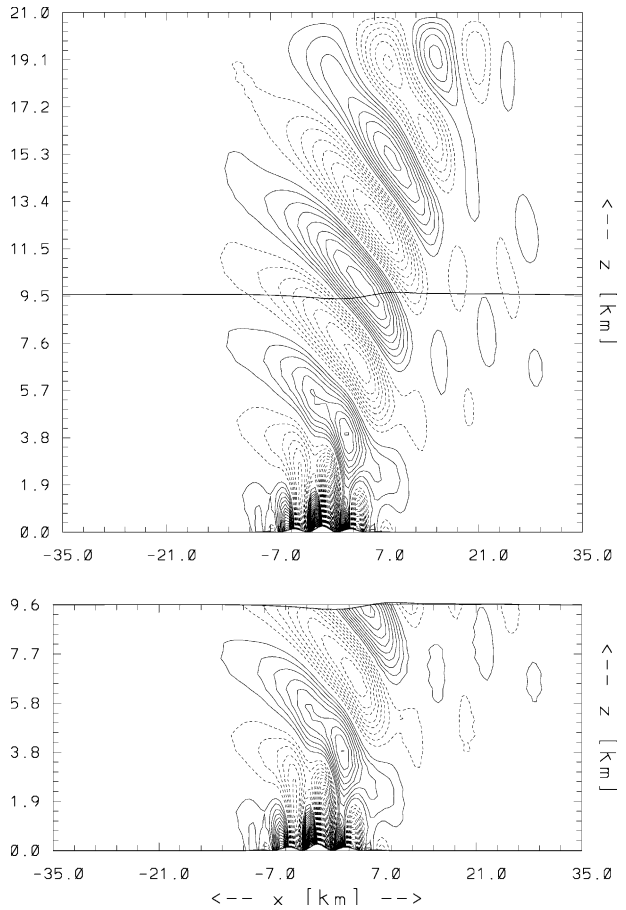

Fig. 2. Vertical velocity for the flow past the terrain profile given in (23) after 5 h of simulation when the fields have essentially reached a steady state. The upper plate represents the reference solution with a sponge layer. The indicated isentropic surface (at an undisturbed height 9.6 km) has been extracted from this run at each time-step and served as the material upper boundary for the reduced-domain simulation shown in the lower plate. The contour interval in both plates is the same as in [26], 0.05 $\mathrm{m\,s^{-1}}$ (zero contour lines not shown).

Fig. 2(b) shows the vertical velocity in the reduced-domain simulation. This solution reproduces the reference result in Fig. 2(a) in the overlapping domain, despite spatial interpolation and finite time-differencing used to determine $H(x,y,t)$ and $\partial H(x,y,t)/\partial t$ from the reference run, and despite the sensitivity of the problem to numerical details [26]. Furthermore, the entire time evolution of both solutions has been found to be the same.

The reduced-domain simulation did not require any absorbing layer or other form of radiative boundary condition, using 36% less CPU time than the reference run. Although designed as a reflexivity test, this experiment appears to indicate the potential for alternative formulations of nonreflective upper boundaries via a generalized (nonstationary) vertical coordinate. This contrasts Grosch and Orszag's [17] conclusions on the uselessness of (stationary) mappings for numerically solving problems in infinite regions. In general, the proposed framework eases the incorporation of any external boundary condition, e.g. by estimating the shape of the upper boundary using auxiliary models, like isentropic models for atmospheric applications, or, as demonstrated in the next example, a shallow-water model for oceanic applications.

3.4. Finite amplitude free surface flow

In principle, our numerical framework enables the specification of the upper surface by arbitrary means (either approximated or exactly prescribed). However, the aim is to use approximations that preserve the computational cost-effectiveness compared to other approaches, while relevant to geo-physical applications. In this example, we document the practicality of incorporating an approximate free-surface boundary in nonhydrostatic ocean models. Our time-dependent coordinate transformation is driven by the solution of the shallow-water equations, a low-order long-wave approximation to free-surface flows; cf. [34] for a discussion. We perform a series of simulations in different flow regimes, to assess the physical applicability of this auxiliary boundary model. Following the methodology in [34,44], we compare the results against "two-layer" simulations with a density ratio 1/1000, defined continuously over a thin interfacial layer within the same fluid.

To accomodate the physics of the problem we solve the incompressible Euler equations

$$\begin{aligned}
&\frac{\partial(\overline{G}\overline{v}^k)}{\partial \overline{x}^k} = 0,\\
&\frac{\mathrm{d}v^j}{\mathrm{d}\overline{t}} = -\frac{1}{\rho}\widetilde{G}^k_j\frac{\partial \phi'}{\partial \overline{x}^k} - g\left(1-\frac{\rho_\mathrm{e}}{\rho}\right)\delta^j_3,\\
&\frac{\mathrm{d}\rho}{\mathrm{d}\overline{t}} = 0,
\end{aligned} \tag{24}$$

where ϕ' denotes the pressure perturbation from a hydrostatically balanced environment characterized by a density profile $\rho_\mathrm{e} = \rho_\mathrm{e}(z)$. In the "two-layer" simulations the profile with a density "discontinuity" at the representative (undisturbed) fluid depth d_0 is prescribed as

$$\rho_\mathrm{e}(z) = \rho_\mathrm{r}\left[1 - 0.5\Delta\rho\left(1+\tanh\frac{z-d_0}{\epsilon}\right)\right], \tag{25}$$

where $\rho_\mathrm{r} = 1$, $\Delta\rho = 0.999$, and $\epsilon = \Delta z$. The reduced domain simulations assume $\rho_\mathrm{e} = \rho_\mathrm{r}$, with a time-dependent upper boundary approximated by the nonlinear hydrostatic shallow-water equations

$$\begin{aligned}
&\frac{\partial d_1}{\partial t} + \frac{\partial(v^j d_1)}{\partial x^j} = 0,\\
&\frac{\mathrm{d}v^j}{\mathrm{d}t} = -g^*\frac{\partial H}{\partial x^j},
\end{aligned} \tag{26}$$

where $\mathrm{d}/\mathrm{d}t = \partial/\partial t + v^j \partial/\partial x^j$ with $j = 1, 2$, the reduced gravity $g^* = g\Delta\rho/\rho_r$ [44] and the density-weighted, normalized fluid depth $d_1 \equiv \rho\overline{G}_0 = \rho(H - z_s)/H_0$. [8] The reduced-domain experiments are complemented with a series of runs using a flat rigid-lid upper boundary, to illustrate the influence of different boundary conditions common in oceanic applications.

All our "two-layer" and reduced-domain experiments simulate the flow past a 2D ridge of the form

$$z_s(x) = z_{s0}\left(1 + (x/a)^2\right)^{-1.5}. \tag{27}$$

The different flow simulations are uniquely characterized by particular choices of the environmental Froude number $F_u = U/\sqrt{gd_0}$, the normalized ridge height z_{s0}/d_0 and the normalized half-width a/d_0. For a given half-width a, the flow regime of a shallow fluid over an obstacle is uniquely determined by F_u and z_{s0}/d_0 [22]. Consequently, ensembles of runs have been performed, categorizing each run with respect to F_u and z_{s0}/d_0. The scenarios summarized in Table 1 are representative of these experiments for the three distinct flow regimes and are marked in the regime diagram, Fig. 3, as in [22,34]. [9] The numerical setup follows [34]. All lengths in the computations are in units of the representative fluid depth d_0 and time is expressed in terms of $\sqrt{d_0/g}$. All simulations assume free-slip at the lower boundary. At the lateral boundaries, the solution is attenuated towards the ambient conditions with an inverse time-scale that increases linearly from 0 at the distance $26\Delta x \approx 2d_0$ to $(16\Delta t)^{-1} \approx (3a/U)^{-1}$ at the boundary. In the "two-layer" simulations the model domain $(x, z) \in [-20d_0, 20d_0] \times [0, 3d_0]$ is resolved with $\mathrm{NX} \times \mathrm{NZ} = 512 \times 96$ uniform grid increments $\Delta x = 5/64$ and $\Delta z = 2/64$. In the (vertically) reduced domain simulations the time-dependent upper boundary is placed at the height of the undisturbed interface layer, equivalent to the representative fluid depth d_0. The semi-Lagrangian option of the model algorithm has been used for these simulations, cf. [34]; whereas the shallow-water Eq. (26) are integrated with the Eulerian NFT scheme [50]. The time-step in both the "two-layer" simulation and the reduced-domain simulation was $\Delta t = 2/64$. The explicit shallow water model was integrated with $1/10\Delta t$ due to thefast surface gravity wave mode.

Fig. 4 compares the flat rigid-lid and the shallow-water approximated upper boundary simulations with the "two-layer" runs, for the different flow regimes summarized in Table 1. Despite the exaggerated bathymetric forcing in our examples – as opposed to bottom profiles typically used in ocean models – the comparison in subcritical, critical, and supercritical conditions shows good agreement between the long-wave approximation to a free-surface and the "two-layer" simulation. In contrast, the flat upper boundary results in a diverse solution throughout the interior domain, impacting the flow not only above the mountain but also upstream and downstream of the obstacle.

Both the sub- and supercritical solutions reach a steady state, whereas under critical conditions the flow is inherently transient [22]. Fig. 5 summarizes the time evolution of a critical flow. It can be seen in the figure as the time progresses that both the upwind propagating bore and the hydraulic lee jump steepen. The detailed comparison deteriorates, but the qualitative behavior of the fluid in the interior of the domain remains in agreement with the "two-layer" simulation. The deterioration is not surprising due to the breakdown of the hydrostatic assumption, underlying the shallow-water equations in (26); cf. [34] for a discussion. To illustrate this effect further, Fig. 6 shows a complete breakdown of the postulated auxiliary boundary model for the (no longer) continuously bounding surface in the special case of a critical flow past a steep mountain (about 50° maximum slope). The observed breakdown does not imply a conceptual shortcoming of the method, but rather indicates the need for more accurate auxiliary boundary models. For example, the generalized-Boussinesq or Green–Naghdi nonhydrostatic equations may be considered for

[8] Here, $d_1 \sim (H - z_s)$; for a discussion linking the incompressible Euler Eq. (24) and the shallow water equations in (26) see [14], chapter 5.6 pp.107.

[9] The solid line in the regime diagram represents Eq. (3.5) in [22], the dashed line dividing region II is found using a multivariate Newton-Raphson method to solve the set of nonlinear algebraic equations (3.8)–(3.17) in [22] for $c_r = 0$.

Table 1
Summary of representative experiments for free surface flows in distinct flow regimes, characterized by the dimensionless Froude number F_u, normalized ridge height z_{s0}/d_0 and normalized half-width a/d_0

Index	Regime	F_u	z_{s0}/d_0	a/d_0	Mountain
1	Subcritical	0.5	0.15	1.875	Gentle
2	Critical	1.0	0.4	1	Steep
3	Critical	1.0	0.4	5	Gentle
4	Critical	0.45	0.5	5	Gentle
5	Supercritical	2.0	0.4	5	Gentle

Table 2
Description of symbols in the text

$\rho;\rho_b;\rho^*;\rho_r$	Density; anelastic density; Jacobian weighted density; reference density	$[kg\,m^{-3}]$
θ	Potential temperature	[K]
θ_b	Reference potential temperature	[K]
θ'	Potential temperature perturbation	[K]
π'	Normalized pressure perturbation	$[m^2\,s^{-2}]$
ϕ'	Pressure perturbation	$[N\,m^{-2}]$
$v^j;u,v,w$	Physical velocity	$[m\,s^{-1}]$
$u_e,v_e,w_e,\rho_e,\theta_e$	Environmental (ambient) profile(s)	
$R;F^j$	rhs; rhs forcing terms in the momentum equation	
$z_s;z_{s0};a$	Surface topography; mountain height; mountain half-width	[m]
$H;H_0$	Height of the top surface, physical system; transformed system	[m]
$x^j;x,y,z,t$	Physical coordinates	
$\bar{x}^j;\bar{x}\equiv E,\bar{y}\equiv D,\bar{z}\equiv C,\bar{t}$	Transformed coordinates	
ζ	Generalized vertical coordinate	
$\overline{v^*}^j;\dot{\bar{x}}^j$	Transformed contravariant velocity components	
$\overline{v^s}^j$	Transformed solenoidal velocity components	
$\overline{G};\overline{G}_0$	Jacobian of the transformation	
$\overline{G}^k_j$	Transformation coefficient j,k	
g^{ij}	i,j element of the conjugate metric tensor of the physical system	
g^*	Reduced gravity	$[m\,s^{-2}]$
$d_1;d_0$	Shallow-water fluid depth; undisturbed depth	[m]
N	Brunt–Väisällä frequency	$[s^{-1}]$
$U;L;T$	Characteristic zonal velocity; length; time	
F_u	Undisturbed Froude number $U/\sqrt{gd_0}$	
δ^k_i	Kronecker-symbol	

higher-order asymptotic approximations, cf. [34]. In some applications it may suffice to regularize boundary discontinuities by artificial dissipation, cf. section 12.10 in [42].

The explicit auxiliary boundary model based on the simple shallow water equations captures the physical nature of finite-amplitude free-surface flows, given a gentle bathymetry (slopes of up to 13° have been successfully tested [10]). This shows the potential for alternative means of incorporating free-surface boundaries in meso-and large-scale oceanic models, where infinitesimal-amplitude surface elevations are typically assumed for simplicity [21]. Given suitable higher-order asymptotic approximations, our approach

[10] In comparison, resolved topographic slopes typically found in operational, high resolution global numerical weather prediction models are about 3–4° (e.g., ECMWF).

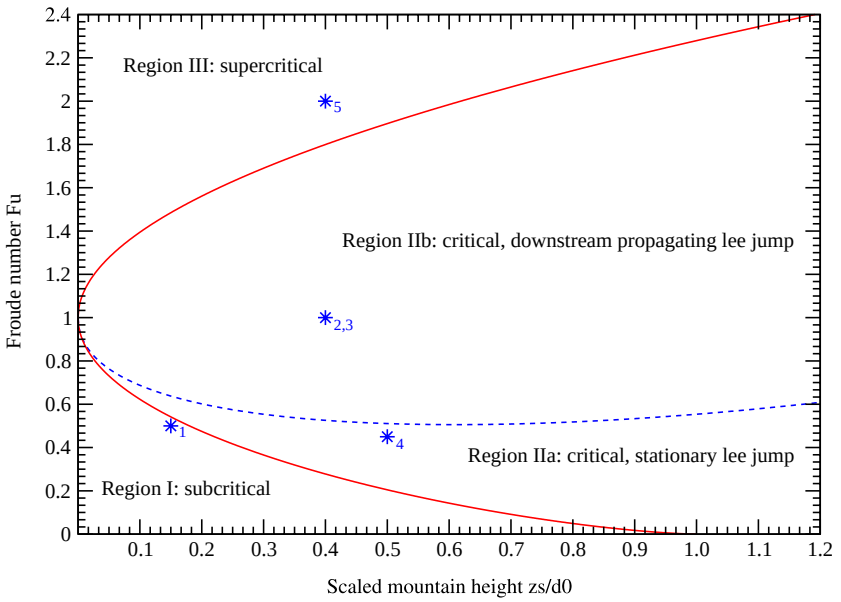

Fig. 3. The regime diagram for the hydrostatic shallow-water equations [22]. The x-axis is the dimensionless ridge height and the y-axis is the undisturbed Froude number $F_u = U/\sqrt{gd_0}$. Region I is entirely subcritical, and the free surface dips symmetrically about the obstacle. Region III is entirely supercritical, and the free surface rises symmetrically about the obstacle after some time. In region IIa, there is an upstream-propagating hydraulic jump and a stationary lee-side hydraulic jump. In region IIb, there is an upstream-propagating and a downstream-propagating hydraulic jump. Parameters corresponding to the 5 cases discussed in this paper are marked with an asterisk ($*$).

may complement inherently implicit methods (in all model variables), [11] typically used in engineering applications involving free-surface flows [6,7].

4. Concluding remarks

We have provided examples of applications relevant to a few distinct areas of computational fluid dynamics, validating both the conceptual and numerical aspects of our time dependent, generalized vertical coordinate transformation. A key feature of this development is the ability to collapse the spatial and temporal variations of the upper and lower boundaries to a single similarity variable (7). This effectively encodes the relationship between an auxiliary boundary model and the interior fluid. In the atmospheric example, the simulation using the height of a selected isentrope in the definition of the vertical coordinate accurately represents the gravity waves generated above the obstacle. In principle, an auxiliary boundary model could have provided the velocity components and potential temperature along a flat boundary, accounting for the changing momentum fluxes across the boundary as the simulation progresses. However, since the shape of the upper boundary is fixed independently of the fluid flow, this approach requires the

[11] Vertical integrals over the nonhydrostatic interior domain are employed to obtain an additional equation for $H(x, y, t)$ while assuming the validity of a hydrostatic representation of pressure in the top layer. Despite the complexity of the resulting implicit formulation, it enables the prediction of the impact of the internal flow on phase and amplitude of surface waves, and vice versa, simultaneously [35].

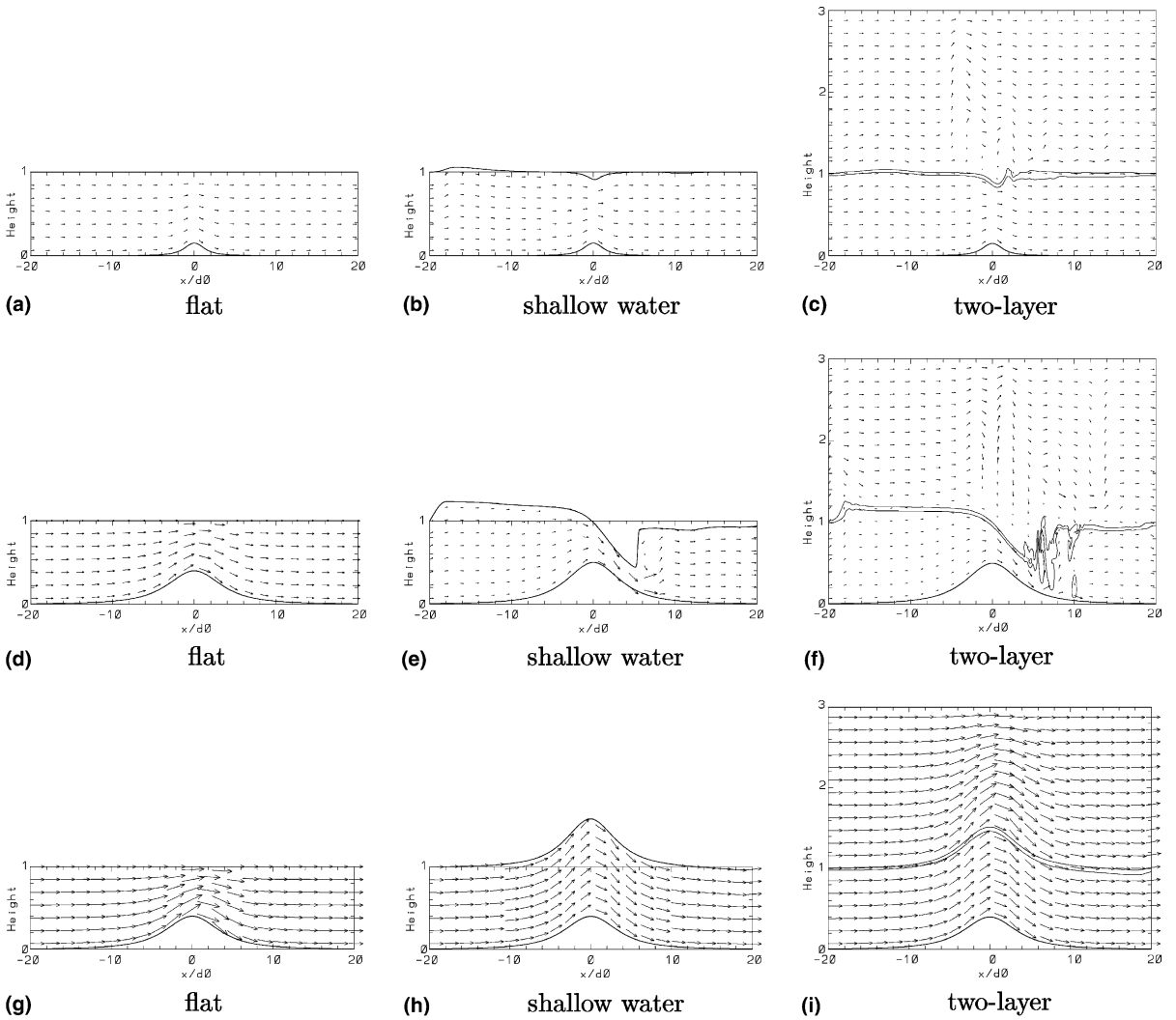

Fig. 4. Summary of the solutions with a gentle slope for subcritical (a)–(c), critical (d)–(f) and supercritical (g)–(i) flow conditions at time $t = 0.5$ (indices 1, 4 and 5 in Table 1, respectively). Results are shown for the simulations with a flat rigid-lid (flat), a predicted shallow-water upper surface (shallow-water) and a "two-layer" simulation (two-layer). The arrow length equal to the distance of two minor x-axis tickmarks is 2. The two contour lines in the two-layer plot are at 0.105 and 0.905 times the density of the lower layer, indicating the position of the density discontinuity between the two layers.

numerically accurate estimation of all dependent variables at the bounding surface. In particular, the specification of advective velocities is more difficult in this case.

In Section 3.4 we successfully demonstrated the practicality of the generalized coordinate transformation for oceanic applications. In this example the free-surface boundary shape is predicted independently, providing the interior fluid model with a Neumann-type boundary condition for pressure, but maintaining the physicality of free-surface flows. While in theory – for incompressible or anelastic models – equivalent Dirichlet and Neumann boundary conditions may be found (cf. [16] for a discussion), the use of a Dirchlet boundary condition can be impractical. In particular in the context of free surface flows, the application of

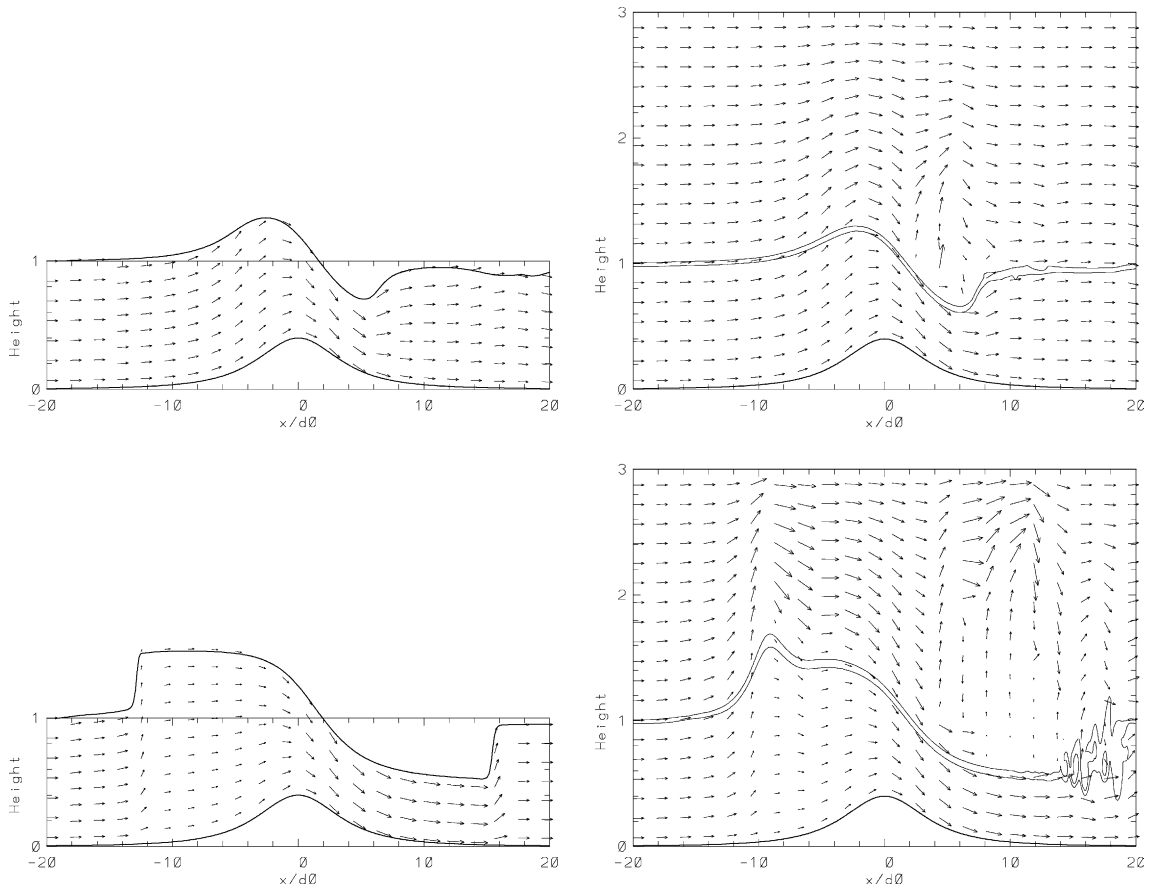

Fig. 5. Time evolution of a critical flow (case 3 in Table 1) at time $t = 0.15$ and $t = 0.5$, respectively, for a predicted shallow-water upper surface (left plates) and a "two-layer" simulation (right plates). Contours and arrow lengths are as in Fig. 4.

a Dirichlet boundary condition for pressure in the numerical solution procedure for the interior domain allows fast propagating surface gravity waves in the solution, which severely limit the time-step. Furthermore, the shape of the upper boundary would remain unknown. Here, the novelty of our approach lies in the coupling of the independent auxiliary boundary model to the interior domain via the proposed vertical coordinate transformation, allowing the use of a larger time-step for the elaborate part of the computations.

In the context of atmospheric applications, where hybrid vertical coordinates are commonly used, our approach may provide an alternative to the vertical nesting of different curvilinear frameworks within the same model. If several vertically bounding surfaces exist, our coordinate transformation may be further generalized to

$$\xi = \sum_{i=1}^{N} \xi_{0i} \frac{z - h_{i-1}}{h_i - h_{i-1}}, \tag{28}$$

with $h_0 = z_s$ and $\xi_{0i} = H_{0i}$ for $h_{i-1} \leqslant z \leqslant h_i$ and 0 otherwise. While this formulation has not been further explored in this paper, it may complement attempts to exploit the strength of different curvilinear frameworks

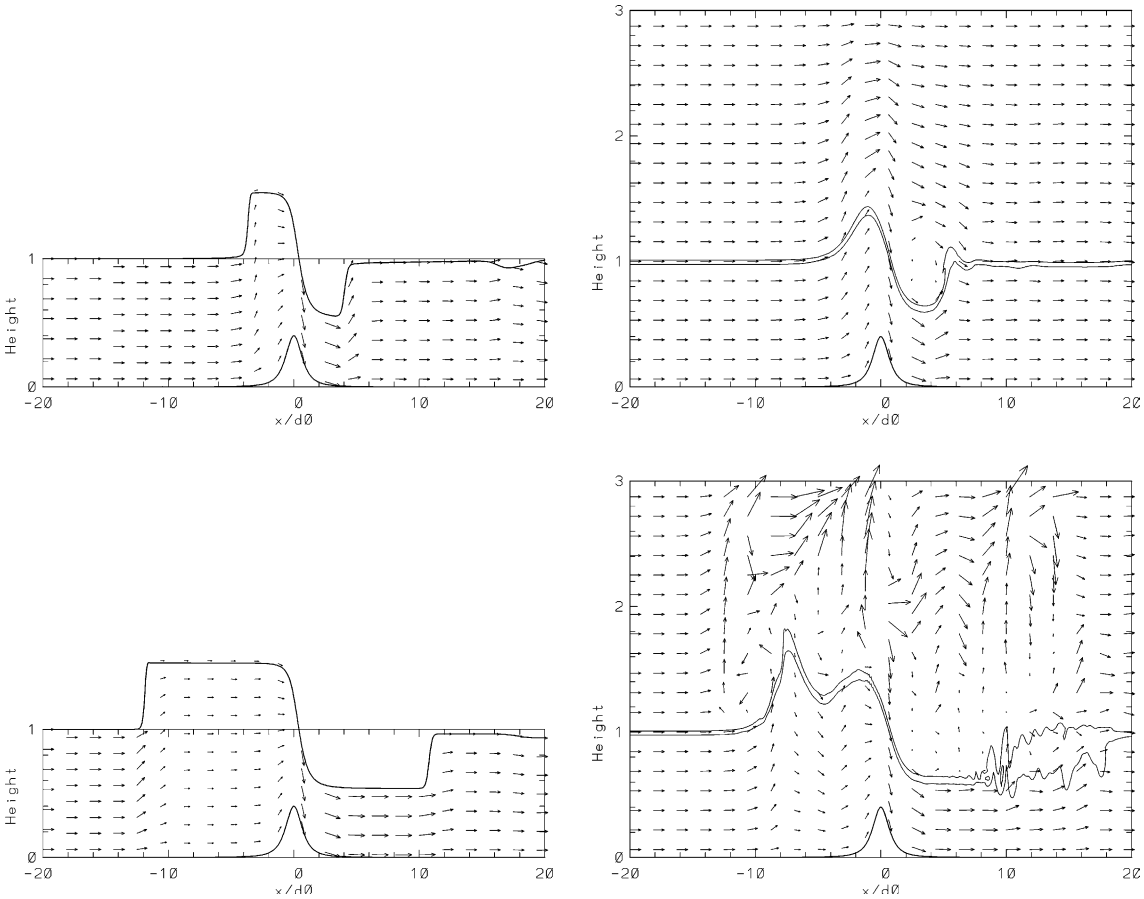

Fig. 6. Solutions for a critical flow past a steep mountain (case 2 in Table 1) at time $t = 0.15$ and 0.5, respectively, for a predicted shallow-water upper surface (left plates) and a "two-layer" simulation (right plates). Contours and arrow lengths are as in Fig. 4.

for various regions of a simulated medium, each coupled through a common interface layer. In particular in geophysical flows, it may facilitate the coupling of boundary layers with stratified fluids, such as the incorporation of mixed layers in deep oceans and the coupling of planetary boundary layers (PBL) to the large-scale dynamic flow.

Acknowledgements

Comments from Matthew Hecht, Anthony Hollingsworth, Martin Miller, Joseph Prusa, and Robert Sharman on an earlier version of this paper helped to improve the presentation. Comments from the two anonymous reviewers were appreciated. This work was supported in part by the Department of Energy "Climate Change Prediction Program" (CCPP) research initiative.

References

[1] D.A. Anderson, J.C Tannehill, R.H. Pletcher, Computational Fluid Mechanics and Heat Transfer, Hemisphere Publ. Corp., New York, 1984.

[2] R. Bleck, Short range prediction in isentropic coordinates with filtered and unfiltered numerical models, Mon. Wea. Rev. 102 (1974) 813–829.
[3] R. Bleck, L.T. Smith, A wind-driven isopycnic coordinate model of the north and equatorial Atlantic Ocean. I: Model development and supporting experiments, J. Geophys. Res. 95C (1990) 3273–3285.
[4] Ph. Bougeault, A non-reflective upper boundary condition for limited-height hydrostatic models, Mon. Wea. Rev. 111 (1983) 229–247.
[5] T. Gal-Chen, C.J. Somerville, On the use of a coordinate transformation for the solution of the Navier–Stokes equations, J. Comp. Phys. 17 (1975) 209–228.
[6] V. Casulli, R.T. Cheng, Semi-implicit finite difference methods for three dimensional shallow water flow, Int. J. Numer. Meth. Fluids 15 (1992) 629–648.
[7] V. Casulli, A semi-implicit finite difference method for non-hydrostatic, free surface flows, Int. J. Numer. Meth. Fluids 30 (1999) 425–440.
[8] P.C. Chu, Two kinds of predictability in the Lorenz system, J. Atmos. Sci. 56 (1999) 1427–1432.
[9] T.L. Clark, A small scale dynamic model using a terrain following coordinate transformation, J. Comp. Phys. 24 (1977) 186–215.
[10] T.L. Clark, R.D. Farley, Severe downslope windstorm calculations in two and three spatial dimensions using anelastic interactive grid nesting: a possible mechanism for gustiness, J. Atmos. Sci. 41 (1984) 329–350.
[11] T.L. Clark, M. Miller, Pressure drag and momentum fluxes due to the Alps. II: Representation in large- scale atmospheric models, Q. J. R. Meteorol. Soc. 117 (1991) 527–552.
[12] J.A. Dutton, The Ceaseless Wind, Dover Publications Inc, 1986.
[13] H. Freudenthal, Dictionary of Scientific Biography, C.C. Gillispie, New York, Scribner & Sons, vol. I–XVI (1970–1980).
[14] A. Gill, Atmosphere–Ocean Dynamics, Academic Press, London, 1982.
[15] D. Givoli, Non-reflecting boundary conditions, J. Comp. Phys. 94 (1991) 1–29.
[16] P. Gresho, R. Sani, On pressure boundary conditions for the incompressible Navier–Stokes equations, Int. J. Numer. Meth. Fluids (1987) 1111–1145.
[17] C. Grosch, S. Orszag, Numerical solution of problems in unbounded regions: coordinate transforms, J. Comp. Phys. 25 (1977) 273–295.
[18] H.-J. Herzog, Testing a radiative upper boundary condition in a nonlinear model with hybrid vertical coordinate, Meteorol. Atoms. Phys. 55 (1995) 185–204.
[19] R.L. Higdon, A two-level time-stepping method for layered ocean circulation models, J. Comput. Phys. 177 (2002) 59–94.
[20] Y.-J.G. Hsu, A. Arakawa, Numerical modeling of the atmosphere with an isentropic vertical coordinate, Mon. Wea. Rev. 118 (1990) 1933–1959.
[21] M. Iskandarani, D.B. Haidvogel, J. Levin, A three-dimensional spectral element model for the solution of the hydrostatic primitive equations, J. Comput. Phys. 186 (2003) 397–425.
[22] D. Houghton, A. Kasahara, Nonlinear shallow fluid flow over an isolated ridge, Comm. Pure Appl. Math. 21 (1968) 1–23.
[23] ISI Web of Science, wos.mimas.ac.uk.
[24] A. Kasahara, Various vertical coordinate systems used for numerical weather prediction, Mon. Wea. Rev. 102 (1974) 509–522.
[25] J.B. Klemp, D.R. Durran, An upper boundary condition permitting internal gravity wave radiation in numerical mesoscale models, Mon. Wea. Rev. 111 (1983) 430–444.
[26] J.B. Klemp, W.C. Skamarock, O. Fuhrer, Numerical consistency of metric terms in terrain-following coordinates, Mon. Wea. Rev. 131 (2003) 1229–1239.
[27] C.S. Konor, A. Arakawa, Design of an atmospheric model based on a generalized vertical coordinate, Mon. Wea. Rev. 125 (1997) 1649–1673.
[28] H. Lamb, Hydrodynamics, sixth ed., Cambridge University Press, New York, London, 1975.
[29] R. Laprise, The Euler equations of motion with hydrostatic pressure as an independent variable, Mon. Wea. Rev. 120 (1992) 197–207.
[30] R. Lindzen, E. Batten, J. Kine, Oscillations in atmospheres with tops, Mon. Wea. Rev. 96 (1968) 133–140.
[31] F.B. Lipps, R.S. Hemler, A scale analysis of deep moist convection and some related numerical calculations, J. Atmos. Sci. 39 (1982) 2192–2210.
[32] R.V. Madala, S.A. Piacsek, A semi-implicit numerical model for baroclinic oceans, J. Comp. Phys. 23 (1977) 167–178.
[33] L.M. Milne-Thomson, Theoretical Hydrodynamics, fifth ed., The MacMillan Press Ltd, 1968.
[34] B.T. Nadiga, L.G. Margolin, P.K. Smolarkiewicz, Different approximations of shallow fluid flow over an obstacle, Phys. Fluids 8 (1996) 2066–2077.
[35] M.M. Namin, B. Lin, R.A. Falconer, An implicit numerical algorithm for solving non-hydrostatic free-surface flow problems, Int. J. Numer. Meth. Fluids 35 (2001) 341–356.
[36] F. Nicoud, T. Schönfeld, Integral boundary conditions for unsteady biomedical CFD applications, Int. J. Numer. Meth. Fluids 40 (2002) 457–465.
[37] N.A. Phillips, A coordinate system having some special advantages for numerical forecasting, J. Meteor. 14 (1957) 184–185.

[38] N.A. Phillips, Dispersion in large scale weather prediction, WMO Sixth IMO lecture 700 (1990) 97.
[39] J.M. Prusa, P.K. Smolarkiewicz, R.R. Garcia, On the propagation and breaking at high altitudes of gravity waves excited by tropospheric forcing, J. Atmos. Sci. 53 (1996) 2186–2216.
[40] J.M. Prusa, P.K. Smolarkiewicz, An all-scale anelastic model for geophysical flows: dynamic grid deformation, J. Comput. Phys. 190 (2003) 601–622.
[41] J.M. Prusa, P.K. Smolarkiewicz, A.A. Wyszogrodzki, Simulations of gravity wave induced turbulence using 512 PE CRAY T3E, Int. J. Appl. Math. Comp. Sci. (2001) 2186–2216.
[42] R.D. Richtmyer, K.W. Morton, Difference Methods for Initial-Value Problems, second ed., Wiley-Interscience, New York, 1967.
[43] B. Riemann, On the hypotheses which lie at the basis of geometry, Nature VIII (May) (1873).
[44] R. Rotunno, P.K. Smolarkiewicz, Vorticity generation in the shallow-water equations as applied to hydraulic jumps, J. Atmos. Sci. 52 (1995) 320–330.
[45] C. Schär, D. Leuenberger, O. Fuhrer, D. Lüthi, C. Girard, A new terrain-following vertical coordinate formulation for atmospheric prediction models, Mon. Wea. Rev. 130 (2002) 2459–2480.
[46] A.J. Simmons, D.M. Burridge, An energy and angular momentum conserving vertical finite difference scheme and hybrid vertical coordinates, Mon. Wea. Rev. 109 (1981) 758–766.
[47] W.C. Skamarock, P.K. Smolarkiewicz, J.B. Klemp, Preconditioned conjugate-residual solvers for Helmholtz equations in nonhydrostatic models, Mon. Wea. Rev. 125 (1997) 587–599.
[48] P.K. Smolarkiewicz, G.A. Grell, A class of monotone interpolation schemes, J. Comput. Phys. 101 (1992) 431–440.
[49] P.K. Smolarkiewicz, J.A. Pudykiewicz, A class of semi-Lagrangian approximations for fluids, J. Atmos. Sci. 49 (1992) 2082–2096.
[50] P.K. Smolarkiewicz, L.G. Margolin, On forward-in-time differencing for fluids: extension to a curvilinear framework, Mon. Wea. Rev. 121 (1993) 1847–1859.
[51] P.K. Smolarkiewicz, L.G. Margolin, On forward-in-time differencing for fluids: an Eulerian/semi-Lagrangian non-hydrostatic model for stratified flows, Atmos. Ocean Special 35 (1997) 127–152.
[52] P.K. Smolarkiewicz, V. Grubišić, L.G. Margolin, A.A. Wyszogrodzki, Forward-in-time differencing for fluids: nonhydrostatic modeling of fluid motions on a sphere, in: Proc. 1998 Seminar on Recent Developments in Numerical Methods for Atmospheric Modeling, Reading, UK, ECMWF, 1999, pp. 21–43.
[53] P.K. Smolarkiewicz, L.G. Margolin, MPDATA: A finite difference solver for geophysical flows, J. Comput. Phys. 140 (1998) 459–480.
[54] P.K. Smolarkiewicz, L.G. Margolin, Variational solver for elliptic problems in atmospheric flows, Appl. Math. Comp. Sci. 4 (1994) 527–551.
[55] P.K. Smolarkiewicz, J.M. Prusa, Forward-in-time differencing for fluids: simulation of geophysical turbulence, in: D. Drikakis, B.J. Guertz (Eds.), Turbulent Flow Computation, Kluwer Academic Publishers, 2002, pp. 207–240.
[56] P.K. Smolarkiewicz, L.G. Margolin, A.A. Wyszogrodzki, A class of nonhydrostatic global models, J. Atmos. Sci. 58 (2001) 349–364.
[57] M.J. Suarez, A. Arakawa, D.A. Randall, Parameterization of the planetary boundary layer in the UCLA general circulation model: formulation and results, Mon. Wea. Rev. 111 (1983) 2224–2243.
[58] K.E. Trenberth, D.P. Stepaniak, A pathological problem with NCEP reanalyses in the stratosphere, J. Climate 15 (2002) 690–695.
[59] L.W. Ucellini, D.R. Johnson, R.E. Schlesinger, An isentropic and sigma coordinate hybrid numerical model: model development and some initial tests, J. Atmos. Sci. 36 (1979) 390–413.
[60] W.T. Welch, P.K. Smolarkiewicz, R. Rotunno, B.A. Boville, The large-scale effects of flow over periodic mesoscale topography, J. Atmos. Sci. 58 (2001) 1477–1492.